

AGN-driven Cold Gas Outflow of NGC 1068 Characterized by Dissociation-Sensitive Molecules

TOSHIKI SAITO ^{1,2} SHURO TAKANO ² NANASE HARADA ^{1,3} TAKU NAKAJIMA ⁴ EVA SCHINNERER ⁵
DAIZHONG LIU ⁶ AKIO TANIGUCHI ⁷ TAKUMA IZUMI ^{1,3} YUMI WATANABE,⁸ KAZUHARU BAMBA ⁸
KOTARO KOHNO ^{9,10} YURI NISHIMURA ^{9,1} SOPHIA STUBER ⁵ AND TOMOKA TOSAKI ¹¹

¹*National Astronomical Observatory of Japan, 2-21-1 Osawa, Mitaka, Tokyo, 181-8588, Japan*

²*Department of Physics, General Studies, College of Engineering, Nihon University, 1 Nakagawara, Tokusada, Tamuramachi, Koriyama, Fukushima, 963-8642, Japan*

³*Department of Astronomy, School of Science, The Graduate University for Advanced Studies (SOKENDAI), 2-21-1 Osawa, Mitaka, Tokyo, 181-1855 Japan*

⁴*Institute for Space-Earth Environmental Research, Nagoya University, Furo-cho, Chikusa-ku, Nagoya, Aichi 464-8601, Japan*

⁵*Max-Planck-Institut für Astronomie, Königstuhl 17, D-69117, Heidelberg, Germany*

⁶*Max-Planck-Institut für Extraterrestrische Physik (MPE), Giessenbachstr. 1, D-85748 Garching, Germany*

⁷*Division of Particle and Astrophysical Science, Graduate School of Science, Nagoya University, Furocho, Chikusa-ku, Nagoya, Aichi 464-8602, Japan*

⁸*Faculty of Symbiotic Systems Science, Fukushima University, Fukushima 960-1296, Japan*

⁹*Institute of Astronomy, School of Science, The University of Tokyo, 2-21-1, Osawa, Mitaka, Tokyo 181-0015, Japan*

¹⁰*Research Center for the Early Universe, School of Science, The University of Tokyo, 7-3-1 Hongo, Bunkyo-ku, Tokyo 113-0033, Japan*

¹¹*Joetsu University of Education, Yamayashiki-machi, Joetsu, Niigata 943-8512, Japan*

(Received May 12, 2022; Revised June 26, 2021; Accepted July 13, 2022)

ABSTRACT

Recent developments in (sub-)millimeter facilities have drastically changed the amount of information obtained from extragalactic spectral scans. In this paper, we present a feature extraction technique using principal component analysis (PCA) applied to arcsecond-resolution ($1''0-2''0 = 72-144$ pc) spectral scan datasets for the nearby type-2 Seyfert galaxy, NGC 1068, using Band 3 of the Atacama Large Millimeter/submillimeter Array. We apply PCA to 16 well-detected molecular line intensity maps convolved to a common 150 pc resolution. In addition, we include the [S III]/[S II] line ratio and [C I] $^3P_1-^3P_0$ maps in the literature, both of whose distributions show remarkable resemblance with that of a kpc-scale biconical outflow from the central AGN. We identify two prominent features: (1) central concentration at the circumnuclear disk (CND) and (2) two peaks across the center that coincide with the biconical outflow peaks. The concentrated molecular lines in the CND are mostly high-dipole molecules (e.g., $H^{13}CN$, HC_3N , and HCN). Line emissions from molecules known to be enhanced in irradiated interstellar medium, CN, C_2H , and HNC, show similar concentrations and extended components along the bicone, suggesting that molecule dissociation is a dominant chemical effect of the cold molecular outflow of this galaxy. Although further investigation should be made, this scenario is consistent with the faintness or absence of the emission lines from CO isotopologues, CH_3OH , and N_2H^+ , in the outflow, which are easily destroyed by dissociating photons and electrons.

Keywords: Active galactic nuclei (16) — Galaxy nuclei (609) — Galaxy winds (626) — Interstellar phases (850) — Molecular gas (1073) — Seyfert galaxies (1447) — Multivariate analysis (1913)

1. INTRODUCTION

Outflows or jets driven by accreting supermassive black holes (active galactic nuclei; AGNs) are considered to play a crucial role in regulating star formation

in massive galaxies, and thus, determine the evolution of galaxies in the universe (e.g., Scannapieco & Oh 2004; Förster Schreiber & Wuyts 2020). In particular, outflows are considered to be capable of quenching star formation activities by heating and/or sweeping dense and cold molecular regions in the interstellar medium (ISM), where stars form (negative AGN feedback; e.g., Sturm et al. 2011; Chen et al. 2022). Thus, galactic cold (neutral atomic and molecular) outflows are important phenomena in galaxy evolution (Veilleux et al. 2020). A recent observational study by Stuber et al. (2021) suggested that a non-negligible number of star-forming galaxies (20%–25%) showed outflow-like features in carbon monoxide (CO) even at redshift = 0.

With the establishment of the Atacama Large Millimeter/submillimeter Array (ALMA), astronomers have started to target lines fainter than the bright CO lines toward nearby galactic cold gas outflows, to inspect their physical and chemical properties (e.g., Aalto et al. 2012; Walter et al. 2017; Aladro et al. 2018; Harada et al. 2018; Michiyama et al. 2020). Concurrently, unbiased spectral line surveys have begun to show the molecular line richness and diversity in extragalactic systems (e.g., Martín et al. 2006; Rangwala et al. 2011; Aladro et al. 2015; Takano et al. 2019; Martín et al. 2021; den Brok et al. 2022; Eibensteiner et al. 2022) as well as in galaxies with known molecular outflow features (e.g., Sakamoto et al. 2021).

With the increase in the number of detected molecular lines and the complex relation between the chemistry and physics behind each molecular line, it is becoming increasingly difficult to interpret line intensities and intensity ratios coherently. To address the increasing complexity, astronomers have utilized a commonly used unsupervised machine learning technique called principal component analysis (PCA; Pearson 1901; Abdi & Williams 2010), and succeeded in reducing the dimensionality, i.e., categorizing and interpreting molecular line diversity (e.g., Costagliola et al. 2011).

Owing to the state-of-the-art high-sensitivity and high angular resolution (sub-)millimeter facilities provided by ALMA, we can currently study the spatial distribution of each molecular line at tens of pc in addition to its line intensity (e.g., Takano et al. 2014; Martín et al. 2021). The number of dimensions and features are continuing to increase. To quantify the morphology of molecular line intensity maps for galaxies, PCA has begun to be applied to the imaging spectral scan datasets of some nearby galaxies (e.g., Meier & Turner 2005; Johnson et al. 2018).

In this paper, we present an application of PCA to high-quality ALMA molecular line maps of the nearby

type-2 Seyfert galaxy NGC 1068 (~ 13.97 Mpc; Anand et al. 2021) captured as part of an imaging spectral scan campaign (Takano et al. 2014; Nakajima et al. 2015; Tosaki et al. 2017; Nakajima et al. in preparation) and to multi-wavelength maps from the literature (Mingozzi et al. 2019; Saito et al. 2022). Subsequently, we describe the outflow features in the central kiloparsec (1-kpc) of NGC 1068 extracted by PCA and present a possible chemistry that coherently explains all PCA results. PCA provides qualitative constraints on the physics and chemistry happening in the center of NGC 1068 based on the morphology of each map. Thus, a quantitative analysis should be done to verify the results of PCA, although it is beyond the scope of this paper.

2. OBSERVATIONS AND PROCESSING

2.1. ALMA observations, ancillary data, and data processing

We conducted an imaging spectral scan at 3 mm toward NGC 1068 using Band 3 of ALMA with its 12-m array (2013.1.00279.S; PI = T. Nakajima). The details of the observations can be found in Nakajima et al. (in preparation). We also downloaded and processed all archival Band 3 data covering NGC 1068 being publicly available as of summer 2021. We focus on data with a spatial resolution of 150 pc or better ($< 2''.08$), which left eight projects (2011.0.00061.S, 2012.1.00657.S, 2013.1.00060.S, 2015.1.00960.S, 2017.1.00586.S, 2018.1.01506.S, 2018.1.01684.S, and 2019.1.00130.S), in addition to 2013.1.00279.S. Some projects have employed observations of the 7-m array and total power array of ALMA. However, for consistency we only used 12-m data, to match the maximum recoverable scale among the detected lines. In addition to the Band 3 data, we used the Band 8 [C I] $^3P_1-^3P_0$ map (2017.1.00586.S; hereafter [C I] map), which traces the cold neutral gas outflow of this galaxy (Saito et al. 2022).

We followed the same procedure from imaging to moment map creation as of Saito et al. (2022). We applied for observatory-delivered calibration with minor manual data flagging using the appropriate CASA version. Subsequently, we reconstructed the images using the PHANGS-ALMA imaging pipeline (Leroy et al. 2021a), which includes several processes. These processes are regridding and concatenating each line visibility data, imaging with single-scale Högbom `clean` (Högbom 1974), primary beam correction, matching spatial resolutions, unit conversion to Kelvin, cube masking, and moment map creation. We note that

Table 1. Line properties and imaging properties

Line	ν_{rest} (GHz)	$\theta_{\text{maj}} \times \theta_{\text{min}}$ ($''$)	V_{ch} (km s^{-1})	σ_{ch} (K)	Med σ_{hex} (K km s^{-1})	SNR_{hex} ($16^{\text{th}}\text{--}50^{\text{th}}\text{--}84^{\text{th}}\text{--max}$)	N_{hex}
(1)	(2)	(3)	(4)	(5)	(6)	(7)	(8)
H ¹³ CN(1–0)	86.339921	0.59×0.52	13.58	0.112	0.89	5.1–14.5–21.9–35.3	21
C ₂ H(1–0)	87.316898	0.56×0.49	6.71	0.146	0.70	5.3–7.0–12.4–18.5	64
HCN(1–0)	88.631602	0.59×0.52	6.61	0.132	0.94	6.3–10.6–26.3–145.6	77
HCO ⁺ (1–0)	89.188525	0.56×0.49	19.65	0.062	1.02	5.4–8.1–16.2–66.9	75
HNC(1–0)	90.663568	2.03×1.74	9.70	0.010	0.28	7.5–14.1–33.2–165.1	77
HC ₃ N(10–9)	90.979023	2.07×1.76	19.33	0.006	0.15	5.8–15.3–34.1–57.5	39
N ₂ H ⁺ (1–0)	93.173977	1.98×1.71	18.87	0.006	0.17	4.9–10.2–21.4–41.9	41
CH ₃ OH(2 _K –1 _K)	96.744550	0.89×0.78	9.85	0.021	0.15	5.3–8.0–16.8–26.8	48
CS(2–1)	97.980953	0.82×0.72	9.72	0.032	0.31	5.8–8.0–19.4–86.2	76
HC ₃ N(11–10)	100.076385	0.57×0.52	17.58	0.045	0.32	5.9–13.9–21.0–34.0	25
HC ₃ N(12–11)	109.173638	0.79×0.70	19.47	0.017	0.24	6.2–16.3–28.6–45.5	24
C ¹⁸ O(1–0)	109.782173	0.82×0.72	9.35	0.021	0.19	4.7–6.9–10.2–17.2	77
¹³ CO(1–0)	110.201354	0.68×0.61	9.98	0.034	0.50	8.2–11.3–17.7–31.8	77
CN(1 _{1/2} –0 _{1/2})	113.191279	0.43×0.38	7.77	0.088	0.64	7.2–11.1–30.3–54.9	55
CN(1 _{3/2} –0 _{1/2})	113.490970	0.43×0.38	7.75	0.168	1.94	5.5–8.9–19.4–50.3	70
CO(1–0)	115.271202	0.40×0.35	0.64	0.801	3.30	18.4–29.5–48.0–77.6	77
[C I](1–0)	492.160651	0.70×0.56	2.38	0.062	1.29	12.6–27.8–89.8–199.5	64

NOTE— Column 1: Line name. Column 2: Rest frequency of line (Endres et al. 2016). Column 3: Major and minor axes (full width at half maximum) of original synthesized beam before convolution to 150 pc ($\sim 2''.08$). Column 4: Velocity resolution. Column 5: Noise root mean square (RMS) at velocity resolution and original synthesized beam size. RMS is measured at each channel, and median value of RMS histogram is listed. This could be different from value listed in Nakajima et al. (in preparation), which summarizes 2013.1.00279.S, because archival ALMA data are added to 2013.1.00279.S, to increase sensitivity of each line. Column 6: Median noise RMS of the detected hexagons. Column 7: Signal-to-noise ratio distribution of the detected hexagons. Column 8: Number of detected hexagons.

we did not attempt any self-calibration. After pipeline imaging, we examined all original data cubes, moment maps, and those maps convolved to a common resolution of 150 pc, basically following the quality assurance strategy described in Leroy et al. (2021a).

Before the pipeline processing, we subtracted the continuum emission in the uv plane. First, we created a dirty map of each spectral window (SPW) for all Band 3 projects, which contains line and continuum emission (a total of 51 SPWs). In this step, the spectral resolution was set to 40 km s^{-1} . Subsequently, we searched all channels, and identified lines detected by the eye. After excluding channels that were $\pm 300 \text{ km s}^{-1}$ near the observed frequencies of the identified lines (systemic velocity was assumed to be 1116 km s^{-1} ; García-Burillo et al. 2014), we subtracted the continuum in the uv plane by fitting a first-degree polynomial function using the CASA task `uvcontsub` based on the sideband of each project.

The outflow velocity measured by the CO(1–0) and [C I] maps is less than $\pm 300 \text{ km s}^{-1}$ (Saito et al. 2022). Note that one sideband typically contains two SPWs. Consequently, we created 26 continuum-subtracted visibility datasets, which were further processed using the imaging pipeline.

The resultant spatial resolution was better than $\sim 2''$ ($\sim 144 \text{ pc}$). The spectral resolution of each molecular line datacube was determined as an integral multiplication of the original channel width and set to be better than 10 km s^{-1} depending on the achievable signal-to-noise ratios. For some fainter lines, such as H¹³CN, we set $< 20 \text{ km s}^{-1}$. For each datacube, we measured the RMS at each channel and then measured the median value, which represents the line sensitivity. The synthesized beam size, channel width, and median noise RMS of the produced datacubes are summarized in Table 1. Here, we only list the lines used for PCA (see

Section 2.2), and the complete list of detected lines can be obtained from Nakajima et al. (in preparation). Note that we only used integrated intensity maps for the analysis described below. Therefore, the spectral resolution choice does not affect the PCA results presented in this paper.

We retrieved the calibrated Multi Unit Spectroscopic Explorer (MUSE/VLT) [S III] $\lambda\lambda$ 9069,9532/[S II] $\lambda\lambda$ 6717,6731 ratio map¹, which traces well the structure of a 1-kpc-scale biconical ionized gas outflow (Mingozi et al. 2019).

2.2. PCA

We convolved all integrated intensity maps and ancillary maps to a 150-pc beam (= 2''08) and subsequently regridded them to a 150-pc-scale hexagonal grid (following, e.g., den Brok et al. 2021), to minimize pixel correlation. When we create the integrated intensity maps, we clipped the datacubes at a signal-to-noise ratio of 4. The 150-pc resolution corresponds to “cloud-scale” (e.g., Leroy et al. 2021b). We directly regridded the [S III]/[S II] ratio map without convolution. An example of the hexagonal maps is shown in Figure 1a. Subsequently, we extracted the central 20'' diameter of NGC 1068 centered at the AGN position (Roy et al. 1998). The extracted part is shown in Figure 1b. This map is colorized to divide the central part into three subregions: circumnuclear disk (“CND”), biconical outflow (“Outflow”), and the remaining part (“Non-outflow”). The outer radius of the CND is ~ 200 pc (e.g., García-Burillo et al. 2014); therefore, the central seven hexagons ($r \sim 225$ pc) cover the entire part of the CND. We used the outline of the biconical outflow defined by Das et al. (2006), which describes well the projected geometry of the cold gas outflow (e.g., Saito et al. 2022). This subregion definition is used in the discussion section (Section 4) but not used for feature extraction using PCA.

Finally, maps with fewer than twenty detected hexagons were removed, resulting in 16 molecular lines: H¹³CN(1–0), C₂H(1–0), HCN(1–0), HCO⁺(1–0), HNC(1–0), HC₃N(10–9), N₂H⁺(1–0), CH₃OH(2_K–1_K), CS(2–1), HC₃N(11–10), HC₃N(12–11), C¹⁸O(1–0), ¹³CO(1–0), CN(1_{1/2}–0_{1/2}), CN(1_{3/2}–0_{1/2}), and CO(1–0) (see Figure 2). The above three steps significantly reduce the number of dimensions and features of the input datasets, and thus, allow PCA to be sensitive to putative faint features around the center of NGC 1068-like cold gas outflows.

Because PCA is not scale-invariant, we standardized all maps before applying PCA, i.e., all input maps had a mean value of zero and a standard deviation of unity. All nondetected hexagons were zero-padded, to match the dimensions. Subsequently, we calculated the covariance matrix and sorted its eigenvectors (or principal component using eigenvalues). The PC values were labeled as PC1, PC2, ..., starting with the largest value. Finally, we evaluated the cumulative contribution rate (CCR) of each PC to determine the amount of variance that the PCs explain. We found that the first two PCs accounted for the majority (90.0%) of the variability in the input maps. Thus, in this study, we considered that PC1 and PC2 can adequately extract gaseous features in the central 1-kpc of NGC 1068 at 150 pc resolution. In Table 2, we list the CCRs up to PC5 and all PC vectors.

3. RESULTS

Figure 3 shows the scatter plot of the first two PC values of each image as well as the feature images of the first two eigenvectors (hereafter PC maps). These data are extracted by applying PCA to 16 integrated intensity maps plus 2 ancillary maps. PC1 is in a direction that maximizes the variance of the projected data, and PC2 has a direction orthogonal to PC1 that maximizes the variance among all directions orthogonal to PC1. Thus, to understand the results of PCA, it is helpful to focus on the observables that show large absolute PC values.

3.1. PC1 represents CND

The most deviated observables in the PC1 direction are HC₃N and H¹³CN(1–0) (positive deviation) and CO isotopologues and [S III]/[S II] ratio (negative deviation). The HC₃N lines are known to be centrally concentrated around the CND at this spatial scale (e.g., Takano et al. 2014). However, CO isotopes (e.g., Tosaki et al. 2017) and the [S III]/[S II] ratio (Mingozi et al. 2019) are known to be spatially extended or not clearly concentrated. These observed trends reported in the literature are consistent with the visual tendencies of the PC1 map. Therefore, PCA extracts the CND itself as the most prominent gaseous feature in the central 1-kpc of NGC 1068. This explanation is supported by the fact that other high-dipole molecules that are also known to coincide with the CND, such as HCN(1–0) and HCO⁺(1–0) (Kohno et al. 2008), show high PC1 values.

The [C I] map shows an approximately zero PC1, potentially because of the presence of bright extended features along the biconical outflow that are extended differently than CO (Saito et al. 2022). Interestingly, a

¹ This is available from the Strasbourg astronomical Data Center (CDS); see <http://cdsarc.u-strasbg.fr/viz-bin/qcat?J/A+A/622/A146>.

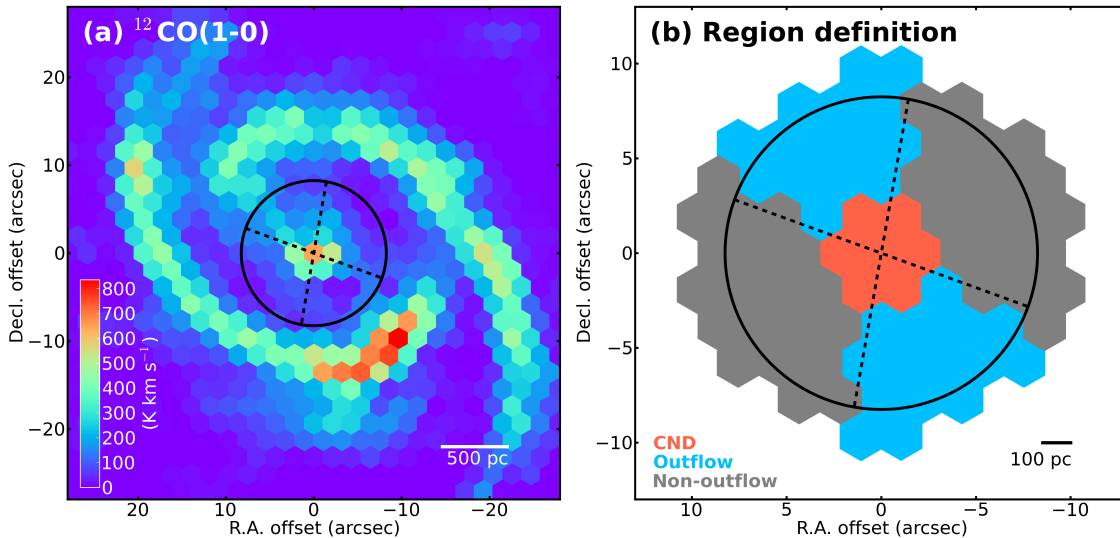


Figure 1. (a) CO(1–0) hexagonally sampled integrated intensity map of the main molecular gas disk of NGC 1068. The two dashed lines crossing the AGN position (Roy et al. 1998) denote the approximate outer edges of the ionized gas cones (Mingozi et al. 2019). The center position of this image is $(\alpha, \delta)_{J2000} = (2h42m40.7132s, -0d00m47.655s)$. The black circle represents the field of view of the [C I] data (i.e., nearly central 1-kpc). (b) Definition of subregions within the central 1-kpc of NGC 1068.

dense gas tracer, $N_2H^+(1-0)$ (e.g., Pety et al. 2017; Kauffmann et al. 2017; Barnes et al. 2020; Tafalla et al. 2021), does not show a high PC1, different from other well-known dense gas tracers.

The molecular line maps that have the highest PC values— $H^{13}CN(1-0)$, HC_3N lines, $HCN(1-0)$, and $HCO^+(1-0)$ —are characterized well by a central concentration. In the top panels of Figure 4, we show four molecular line maps, that have the highest PC1 values, divided by the CO(1–0) map, and corresponding PC2 maps are shown in the bottom panel. Here $HC_3N(10-9)$ represents the other HC_3N maps as these have similar PC1 and PC2 values. The line ratio maps still show the central concentration in comparison with the corresponding line ratio maps that have the highest PC2 values.

3.2. PC2 represents outflow

As noticeable in Figure 3(a), the second-most prominent feature extracted by PCA is highly positively correlated with the [S III]/[S II] ratio map. This map displays a metallicity-independent ionization parameter distribution (Mingozi et al. 2019). In the case of the NGC 1068 center, it probably traces the biconical ionized gas outflow. The second-most deviated observable in the PC2 direction is the [C I] map. Saito et al. (2022) have shown that [C I] gas traces the biconical feature along the outflow, and thus PC2 probably extracts a biconical feature along the outflow direction. This is consistent with the visual tendency of the PC2 map (Figure 3c), which

shows two symmetric peaks a few hundred parsecs away from the AGN position.

The $CN(1_{3/2}-0_{1/2})$, $C_2H(1-0)$, $HNC(1-0)$, and $CN(1_{1/2}-0_{1/2})$ molecular line maps (Figure 2) and their line ratio maps (Figure 3) are similar to the PC2 map. Interestingly, all radicals used in PCA are selected. The remaining molecule, HNC, is also a unique molecule among the input molecules because it is an isomer of HCN. In Section 4, we discuss plausible explanations for the enhancement of these molecules in the AGN outflow of NGC 1068, as well as for the lower PC2 maps, i.e., CO isotopes, $CH_3OH(2_K-1_K)$, and $N_2H^+(1-0)$.

We note that a bright spot in the north-eastern pixel of the $^{13}CO(1-0)$, $C^{18}O(1-0)$, and $CO(1-0)$ (Figure 2) is probably a part of the northern bar-end (Figure 1a). This spot is not captured in the PC1 and PC2 maps, and thus this is not the primary reason why these molecules systematically show lower PC1 and PC2 values. Apart from this, the bar itself may affect the PCA with 150 pc resolution maps (see the molecular bar presented in García-Burillo et al. 2014), although it is reported that the [C I] and [S III]/[S II] ratio maps mainly trace the outflow, not the bar (Mingozi et al. 2019; Saito et al. 2022). Differentiating the bar from the outflow should be done with higher angular resolution data. In this paper we regard that the PC2 map represents the outflow.

4. DISCUSSION

Here, we discuss a possible mechanism that can explain all above-mentioned trends.

Table 2. cumulative contribution rates and all PC vectors up to PC5 ordered by PC2 values

	PC1	PC2	PC3	PC4	PC5
CCR	0.69	0.90	0.97	0.98	0.99
[S III]/[S II] ratio	-1.53	2.80	2.50	-0.23	0.08
[C I](1-0)	-0.09	1.96	-2.55	-2.00	-0.28
CN($1_{3/2}$ - $0_{1/2}$)	0.39	0.56	-0.50	0.89	0.86
C ₂ H(1-0)	-0.19	0.50	-0.62	2.44	-2.74
HNC(1-0)	0.49	0.36	-0.25	0.78	0.89
CN($1_{1/2}$ - $0_{1/2}$)	0.62	0.35	-0.75	0.90	0.41
HCN(1-0)	0.81	0.09	-0.04	0.48	1.34
CS(2-1)	0.28	-0.10	-0.40	-0.36	0.06
HCO ⁺ (1-0)	0.45	-0.11	0.10	1.25	1.14
H ¹³ CN(1-0)	1.10	-0.34	0.61	-0.65	1.06
HC ₃ N(10-9)	1.01	-0.43	0.61	-0.47	-0.40
HC ₃ N(12-11)	1.07	-0.43	0.69	-1.07	-0.55
HC ₃ N(11-10)	1.04	-0.51	0.90	-1.27	-1.85
CH ₃ OH(2_K - 1_K)	-0.44	-0.67	-0.84	-0.32	-0.50
CO(1-0)	-1.40	-0.74	-0.30	-0.05	0.20
N ₂ H ⁺ (1-0)	0.19	-0.88	0.92	0.33	-0.36
¹³ CO(1-0)	-1.94	-1.12	-0.06	-0.15	0.35
C ¹⁸ O(1-0)	-1.86	-1.29	-0.11	-0.49	0.28

Based on observational studies in the literature, a kpc-scale biconical structure driven by a radio jet (e.g., Gallimore et al. 1996a,b) is considered to penetrate the disk plane (e.g., Schinnerer et al. 2000; Das et al. 2006; García-Burillo et al. 2014, 2019). The biconical structure is likely driven by a jet-driven expanding bubble which heats the surrounding ISM and creates shocks resulting in multiphase outflows (see also numerical simulations done by Mukherjee et al. 2016). By its strong ultraviolet (UV) and X-ray radiation fields as well as large-scale shocks (e.g., Barbosa et al. 2014; May & Steiner 2017), this outflowing bicone naturally causes photo- and shock-dissociation (e.g., García-Burillo et al. 2017; Saito et al. 2022) and ionization (e.g., Mingozzi et al. 2019) of molecular clouds within the disk. We suggest that the mechanism of molecular enhancement/suppression can be explained by dissociative processes occurring in the biconical outflow. Here, we discuss individual molecules in this context.

4.1. Molecules enhanced in outflow

C₂H enhancement: Enhancement in C₂H(1-0) in the outflow of NGC 1068 was previously reported in García-Burillo et al. (2017) using high-angular resolution ALMA datasets. Based on chemical modeling, the authors concluded that the observed high abun-

dance of C₂H can only be achieved in a dense molecular gas heavily irradiated by UV/X-ray photons and/or in icy mantle sputtering due to shocks driven by the jet-ISM interaction. These processes dissociate CO and release C atoms and C⁺ ions, which are used to form C₂H (e.g., Fuente et al. 1993). This CO dissociation scenario is preferable for explaining the observed high C₂H(1-0)/CO(1-0) ratio distribution (Figure 4) and the observed high [C I]/CO ratio distribution within the outflow of NGC 1068 (Saito et al. 2022). Figure 5 shows the maximum value of the integrated line intensity divided by the CO(1-0) line integrated intensity in the three specific regions shown in Figure 1b. In the “Outflow”, the C₂H(1-0)/CO(1-0) ratio is ~0.6 dex higher than in the “Non-outflow”. In the case of the [C I]/CO ratio, the difference is almost an order of magnitude. Both trends quantitatively support the CO dissociation scenario, which results in bright C₂H(1-0) and [C I](1-0) lines in the outflow.

According to the regions defined in Figure 1b, the lines in Figure 5 are ordered by the maximum ratio in the “Outflow” divided by the maximum ratio in the “Non-outflow”. Thus, the lines on the right-hand (left-hand) side tend to be enhanced (suppressed) in the “Outflow” region. This order is similar to that by the PC2 values

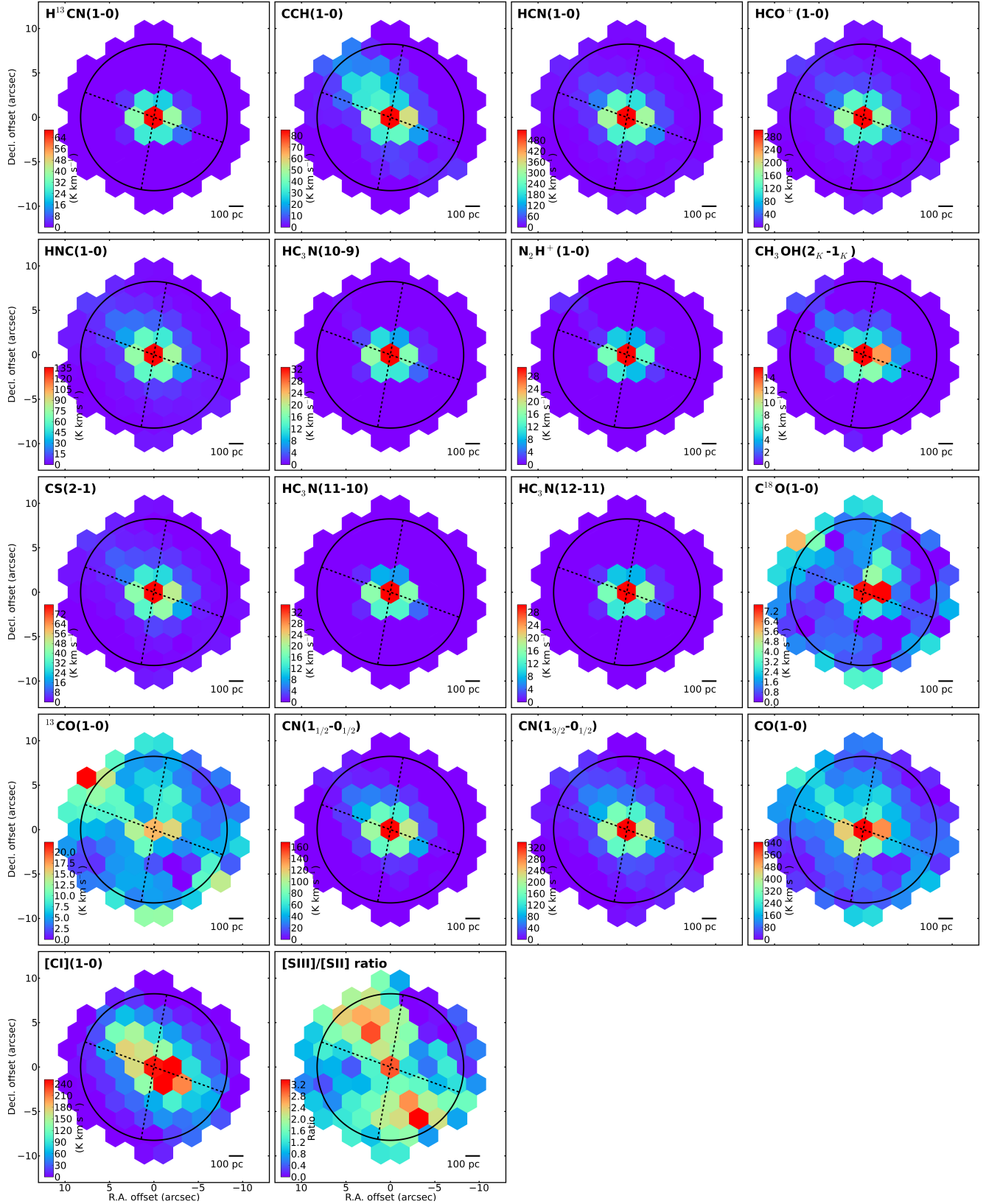


Figure 2. Image gallery of 16 well-detected 3-mm molecular lines in the central 1-kpc of NGC 1068 (top 16 rows) and two ancillary maps ([C I] and [S III]/[S II] ratio), which are known to trace the biconical outflow structure. In the top-left corner of each panel, name of the atomic and molecular line and number of detected pixels are presented. Two dashed lines crossing the AGN position (Roy et al. 1998) denote approximate outer edges of the ionized gas cones (Mingozzi et al. 2019). The black circle represents the field of view of the [C I] data (i.e., nearly the central 1-kpc).

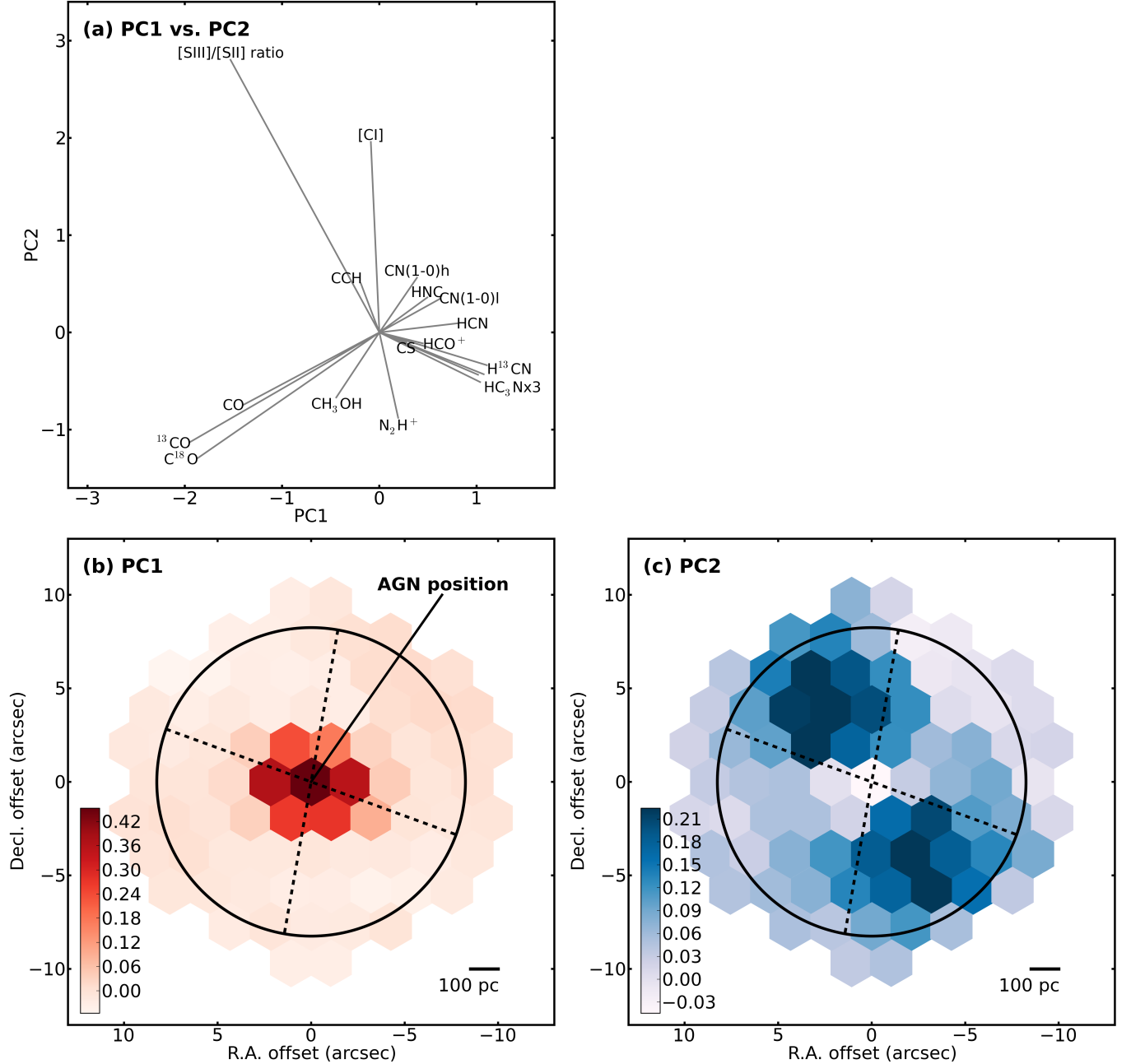


Figure 3. (a) The scatter plot of first two PCs of each image. Each PC is extracted by applying PCA to 16 molecular line maps and two ancillary maps ([S III]/[S II] ratio and [C I] intensity). PC maps are PC1 (b) and PC2 (c). Two dashed lines crossing AGN position (Roy et al. 1998) denote approximate outer edges of ionized gas cones (Mingozi et al. 2019). Circle represents approximate field of view of Band 8 [C I] map (Saito et al. 2022), which has the smallest FoV among the maps described in this paper.

(see Table 2), and thus, supports the results of PCA in a complementary manner.

CN enhancement: A similar explanation to C₂H(1-0) above (except for the dust sputtering) can be used for the CN enhancement. CN is considered to primarily form from the photodissociation of HCN and neutral-neutral reactions with some molecules (e.g., Aalto et al.

2002). The production efficiency of CN is highly dependent on the number of free C atoms and C⁺ ions in the case of neutral-neutral reactions such as CH + N → CN + H, which is considered as one of the most important reaction pathways to CN in diffuse PDR, i.e., irradiated ISM (e.g., Fuente et al. 1993; Boger & Sternberg 2005). Thus, CN abundance can be enhanced in a

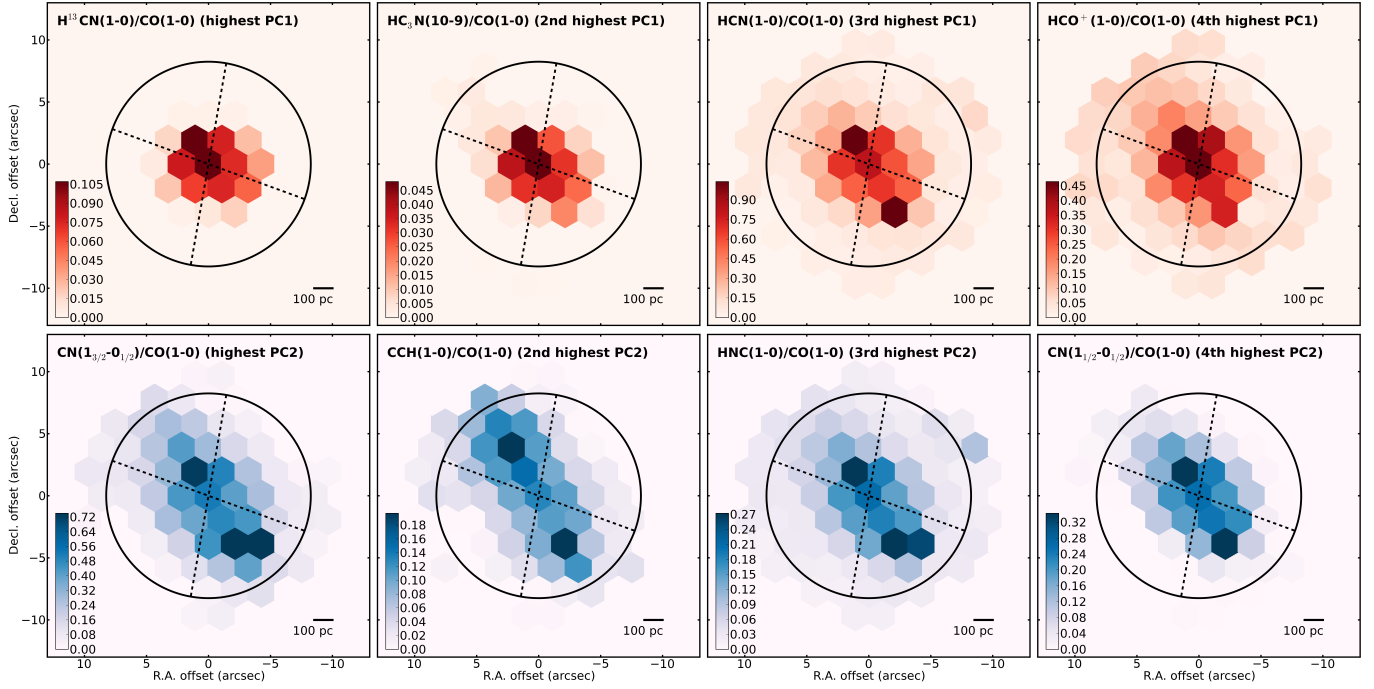


Figure 4. (top) Four highest and most lowest PC1 maps divided by CO(1-0) map as determined by PCA. (bottom) Corresponding PC2 maps.

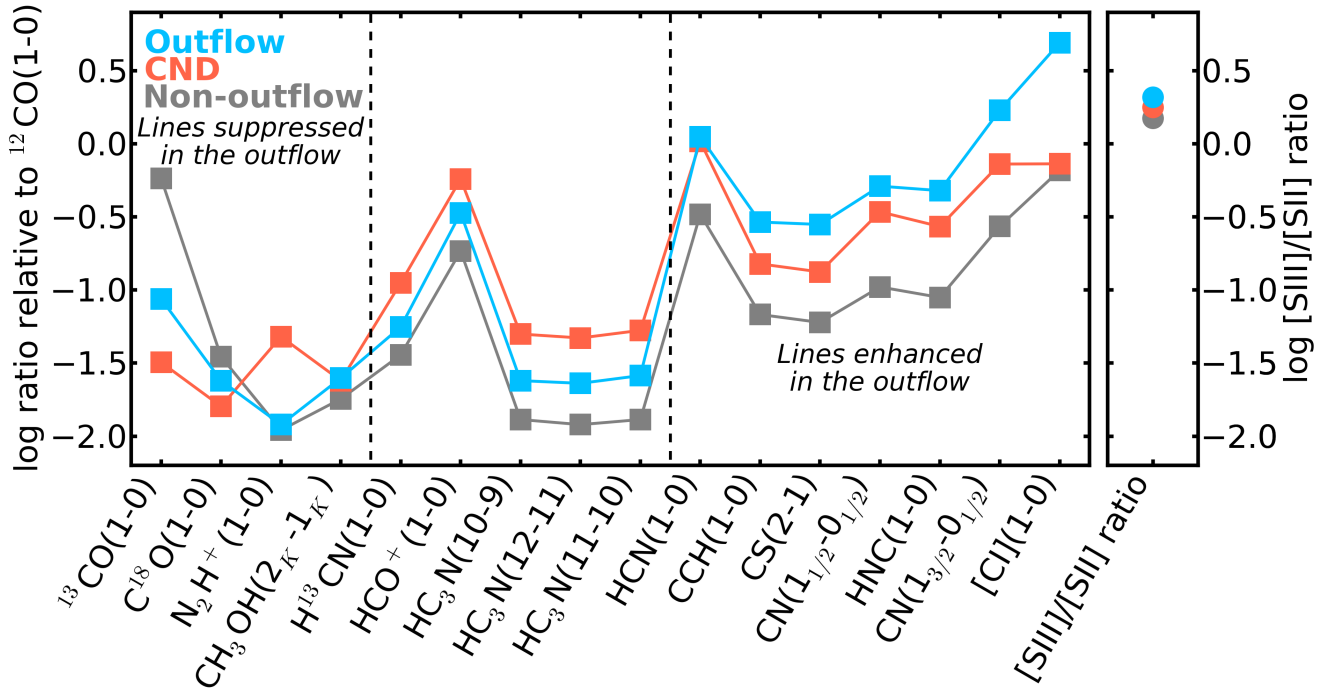


Figure 5. Integrated line intensities relative to CO(1-0) integrated intensity in each subregion within the central 1-kpc of NGC 1068. Here, we plot the maximum ratio within each subregion. Lines are ordered by differences between “Outflow” (blue) and “Non-outflow” (grey), i.e., lines on the right-hand (left-hand) side are enhanced (suppressed) in outflow. In the right panel, we plot the [S III]/[S II] ratio for reference. This order is similar to that by PC2 values, supporting that emission lines positively correlated to PC2 map are enhanced in the outflow.

molecular gas irradiated by UV/X-ray radiation. Based

on PCA and Figure 5, both CN hyperfine transitions

are enhanced in the “Outflow” region compared to the HCN line, which supports the dissociation-enhanced CN scenario in the cold gas outflow. A similar CN enhancement is reported in the cold gas outflow of the nearest ULIRG QSO Mrk 231 (Cicone et al. 2020).

HNC enhancement: Based on PCA, the HNC map is more positively correlated with the PC2 map than the HCN map, although the statistical difference is small. Based on Figure 5, the HNC/CO difference between “Outflow” and “Non-outflow” is ~ 0.8 dex, which is larger than the HCN/CO difference of ~ 0.5 dex. Thus, both analyses suggest that HNC is more enhanced in the outflow than HCN.

The HNC/HCN ratio is observationally known to correlate with the gas kinetic temperature (decreasing ratio with increasing gas temperature due to different energy levels and an isomerization barrier; e.g., Hacar et al. 2020). However, in irradiated ISM, free electrons play a crucial role in enhancing the HNC/HCN ratio to approximately unity by the dissociative recombination (DR) of HCNH^+ (e.g., Herbst et al. 2000). The same scenario was proposed by Aalto et al. (2002) to explain the observed high HNC/HCN intensity ratio for nearby luminous infrared galaxies. As the DR can produce HNC and HCN with almost equal branching ratios (e.g., Mendes et al. 2012), the observed abundance ratio also becomes almost unity. Thus, we suggest that the high HNC/HCN ratios within the bicone of NGC 1068 are driven by the DR of HCNH^+ , i.e., dissociation enhancement of HNC. Although this scenario should be further investigated using higher quality observational data, this fits well with the explanations for the other enhanced molecules, discussed above. Note that CN can also be formed in the DR of HCNH^+ (e.g., Herbst 1995), which is another possible explanation to the enhancement of CN in the “Outflow.”

4.2. Molecules suppressed in outflow

CO suppression: The gas-phase abundance of CO and its isotopologues is controlled by photodissociation caused by UV photons (e.g., Visser et al. 2009) and shock dissociation (e.g., Hollenbach & McKee 1980). The destruction of CO and the production of C atoms are revealed in the outflow of NGC 1068 (Saito et al. 2022) and other galaxies (e.g., Cicone et al. 2018; Izumi et al. 2020). Considering isotope-selective photodissociation (i.e., less abundant molecules are less self-shielded; e.g., Bally & Langer 1982), the CO isotopologues are also expected to be destroyed even with higher dissociation rates. The dissociation-suppressed scenario naturally suggests a strong anti-correlation between the CO maps and the PC2 map (see also Table 2).

CH₃OH suppression: Gas-phase CH_3OH becomes abundant when interstellar icy mantles rich in CH_3OH are sublimed by radiation or shock heating (e.g., Viti et al. 2011), whereas the suppression of CH_3OH is expected in clouds irradiated by a strong UV radiation field without shielding ($A_v \sim 5$; Martín et al. 2009). In the case of NGC 1068’s center, the CH_3OH map anti-correlates with the PC2 map, i.e., CH_3OH is suppressed in the outflow. However, this does not necessarily indicate the absence of shocks, as shock-enhanced CH_3OH can be rapidly destroyed by UV radiation. Radiation heating and shock heating are expected to coexist in jet-driven multi-phase outflows, as shown by different molecular and atomic line observations (García-Burillo et al. 2017; Saito et al. 2022) and numerical simulations of jet–ISM interaction phenomena (e.g., Mukherjee et al. 2016). Thus, we suggest that shock CH_3OH enhancement may occur in the outflow. However, dissociation suppression dominates.

Dissociative high-speed shocks might be expected to destroy molecules, leading to the suppression of CH_3OH (e.g., Hollenbach & McKee 1980). However, in this case, most molecules other than CH_3OH are also destroyed, which is inconsistent with the molecular-rich nature of the NGC 1068 outflow. Thus, we suggest that “non-dissociative shocks and dissociative UV/X-ray radiation” best probably describe the chemistry of the cold gas outflow of NGC 1068. This is consistent with conclusions based on high-spatial resolution $\text{C}_2\text{H}(1-0)$ observations (García-Burillo et al. 2017).

N₂H⁺ suppression: Similar to the DR of HCNH^+ , its reaction with free electrons dissociates N_2H^+ . Thus, if free electrons play an important role in enhancing HNC, the dissociation suppression of N_2H^+ (and another molecular ion HCO^+) is plausible. A large number of free electrons in the outflow are expected, based on the high $[\text{S III}]/[\text{S II}]$ ratio along the bicone (Mingozzi et al. 2019). However, reactions with neutral molecules and molecular ions and the effect of cosmic rays are also important for understanding the chemistry of these molecular ions, not only DR. Thus, accurate column density measurements (e.g., Nakajima et al. 2018) and complex chemical modeling (e.g., as done by Harada et al. 2021) are required to further constrain the behavior of molecular ions in the cold gas outflow of NGC 1068.

4.3. Molecules enhanced/suppressed in CND

As briefly described above, molecules concentrated to the CND are high-dipole molecules. Molecules negatively correlated are CO and its isotopologues which are easily destroyed by UV photons and X-rays. These

trends support the findings reported in [Takano et al. \(2014\)](#), i.e., the CND contains regions where HC_3N molecules are effectively shielded from the strong AGN radiation. The different correlation strength among the input maps may imply the chemistry and physics around the central AGN (e.g., X-ray dominated chemistry, shock chemistry, and high-temperature chemistry; [Meijerink & Spaans 2005](#); [Harada et al. 2013](#); [Izumi et al. 2013](#); [Huang et al. 2022](#)). For the bright central region of NGC 1068, constraining the excitation of these molecules with higher angular resolution data is an interesting future direction.

[Huang et al. \(2022\)](#) recently reported that the molecular gas outflow in the CND is shock-driven. Thus, interestingly, the putative jet-ISM interaction between the radio jet and the CND naturally explains their findings within the CND and our findings outside the CND consistently. This further supports the results of the PCA and our interpretation described in this paper.

5. SUMMARY

In this paper, we present our 150-pc-resolution ALMA Band 3 spectral scans for the central kpc of the nearby type-2 Seyfert galaxy, NGC 1068, supplemented with archival Band 3 datasets. To characterize lines related to the cold gas outflow of this galaxy, we employ the PCA algorithm and successfully categorized the detected lines into (1) lines related to the CND and (2) lines related to the outflow.

We find that the lines enhanced in the CND are mostly high-critical density tracers (e.g., H^{13}CN , HC_3N , and HCN), whereas those in the outflow are CN , C_2H , HNC , and possibly HCN . We also find that CO and its isotopologues, CH_3OH , and N_2H^+ are suppressed in the outflow.

We suggest that all enhanced and suppressed molecules currently detected in the cold gas outflow can be explained by a coherent scenario: non-dissociative shocks and dissociative UV/X-ray radiation driven by the jet-ISM interaction. Thus, we provide observational evidence of how negative AGN feedback occurring in the central 1-kpc of a galaxy chemically changes the molecular ISM of the host galaxy. However, our discussions rely on fluxes and flux ratios, and thus, we need accurate column density measurements and complex chemical modeling to provide quantitative constraints on this scenario.

To emphasize the large-scale structure in the central 1-kpc, we degrade the original molecular line intensity maps. This allows PCA to find a faint extended structure along the well-known biconical outflow from the input maps. However, higher angular resolution and

higher sensitivity maps are required to accurately understand the effects of the negative AGN feedback, i.e., the changes in the molecular clouds affected by the AGN outflow.

Finally, we note that the results of PCA described in this paper change, when the sensitivity and angular resolution of the input data improve. Especially, molecules with less number of detected hexagons are more affected. The explanations for these molecules should be read with caution.

This work was supported by NAOJ ALMA Scientific Research Grant Numbers 2021-18A. NH acknowledges support from JSPS KAKENHI Grant Number JP21K03634. KK acknowledges support from JSPS KAKENHI Grant Number JP17H06130. The work of YN was supported by NAOJ ALMA Scientific Research Grant Numbers 2017-06B and JSPS KAKENHI grant Number JP18K13577. The work of KB was supported in part by the JSPS KAKENHI Grant Number JP21K03547. TT acknowledges support from JSPS KAKENHI Grant Number JP20H00172 and NAOJ ALMA Scientific Research Grant Numbers 2020-15A. This work was supported by NAOJ ALMA Scientific Research Grant Numbers 2021-18A. We would like to thank Editage (www.editage.com) for English language editing. This study was supported by NAOJ ALMA Scientific Research Grant Number 2021-18A. This paper makes use of the following ALMA data: ADS/JAO.ALMA#2011.0.00061.S, ADS/JAO.ALMA#2012.1.00657.S, ADS/JAO.ALMA#2013.1.00060.S, ADS/JAO.ALMA#2013.1.00279.S, ADS/JAO.ALMA#2015.1.00960.S, ADS/JAO.ALMA#2017.1.00586.S, ADS/JAO.ALMA#2018.1.01506.S, ADS/JAO.ALMA#2018.1.01684.S, and ADS/JAO.ALMA#2019.1.00130.S. ALMA is a partnership of ESO (representing its member states), NSF (USA) and NINS (Japan), together with NRC (Canada), MOST and ASIAA (Taiwan), and KASI (Republic of Korea), in cooperation with the Republic of Chile. The Joint ALMA Observatory is operated by ESO, AUI/NRAO and NAOJ. This research has made use of the NASA/IPAC Extragalactic Database (NED), which is funded by the National Aeronautics and Space Administration and operated by the California Institute of Technology. The National Radio Astronomy Observatory is a facility of the National Science Foundation operated under cooperative agreement by Associated Universities, Inc. This research has made use of the SIMBAD database, operated at CDS, Strasbourg, France. Data analysis was in part carried out on the Multi-wavelength Data Analysis System operated by the Astronomy Data Center (ADC), National Astronomical Observatory of Japan.

Software: ALMA Calibration Pipeline, Astropy (Astropy Collaboration et al. 2013, 2018), CASA (McMullin et al. 2007), NumPy (Harris et al. 2020), PHANGS-ALMA Pipeline (Leroy et al. 2021a), SciPy (Virtanen et al. 2020), spectral-cube (Ginsburg et al. 2019), radio-beam

APPENDIX

A. OTHER MINOR FEATURE MAPS EXTRACTED BY PCA

Here we describe three PC maps that account for the minor fraction (10.0%) of the variability in the input 18

maps (Figure 6). PC3 probably captures a peak at the AGN position. However, the explanation is not straightforward because extended emission also show positive

values. PC4 shows a positive blob in the south and a negative blob in the north. Interestingly, two maps showing outflow-like features ($[C\ I]$ and $C_2H(1-0)$) are classified as the most positively and negatively corre-

lated maps. This may imply the chemical difference in the northern and southern part of the outflow, although note that PC4 and PC5 only account for 2% of the variability in the input maps. Higher angular resolution maps are useful to uncover these possible features.

REFERENCES

- Aalto, S., Garcia-Burillo, S., Muller, S., et al. 2012, *A&A*, 537, A44, doi: [10.1051/0004-6361/201117919](https://doi.org/10.1051/0004-6361/201117919)
- Aalto, S., Polatidis, A. G., Hüttemeister, S., & Curran, S. J. 2002, *A&A*, 381, 783, doi: [10.1051/0004-6361:20011514](https://doi.org/10.1051/0004-6361:20011514)
- Abdi, H., & Williams, L. J. 2010, *Wiley interdisciplinary reviews: computational statistics*, 2, 433
- Aladro, R., Martín, S., Riquelme, D., et al. 2015, *A&A*, 579, A101, doi: [10.1051/0004-6361/201424918](https://doi.org/10.1051/0004-6361/201424918)
- Aladro, R., König, S., Aalto, S., et al. 2018, *A&A*, 617, A20, doi: [10.1051/0004-6361/201833338](https://doi.org/10.1051/0004-6361/201833338)
- Anand, G. S., Lee, J. C., Van Dyk, S. D., et al. 2021, *MNRAS*, 501, 3621, doi: [10.1093/mnras/staa3668](https://doi.org/10.1093/mnras/staa3668)
- Astropy Collaboration, Robitaille, T. P., Tollerud, E. J., et al. 2013, *A&A*, 558, A33, doi: [10.1051/0004-6361/201322068](https://doi.org/10.1051/0004-6361/201322068)
- Astropy Collaboration, Price-Whelan, A. M., Sipőcz, B. M., et al. 2018, *AJ*, 156, 123, doi: [10.3847/1538-3881/aabc4f](https://doi.org/10.3847/1538-3881/aabc4f)
- Bally, J., & Langer, W. D. 1982, *ApJ*, 255, 143, doi: [10.1086/159812](https://doi.org/10.1086/159812)
- Barbosa, F. K. B., Storchi-Bergmann, T., McGregor, P., Vale, T. B., & Rogemar Riffel, A. 2014, *MNRAS*, 445, 2353, doi: [10.1093/mnras/stu1637](https://doi.org/10.1093/mnras/stu1637)
- Barnes, A. T., Kauffmann, J., Bigiel, F., et al. 2020, *MNRAS*, 497, 1972, doi: [10.1093/mnras/staa1814](https://doi.org/10.1093/mnras/staa1814)
- Boger, G. I., & Sternberg, A. 2005, *ApJ*, 632, 302, doi: [10.1086/432864](https://doi.org/10.1086/432864)
- Chen, Z., He, Z., Ho, L. C., et al. 2022, *Nature Astronomy*, doi: [10.1038/s41550-021-01561-3](https://doi.org/10.1038/s41550-021-01561-3)
- Cicone, C., Maiolino, R., Aalto, S., Muller, S., & Feruglio, C. 2020, *A&A*, 633, A163, doi: [10.1051/0004-6361/201936800](https://doi.org/10.1051/0004-6361/201936800)
- Cicone, C., Severgnini, P., Papadopoulos, P. P., et al. 2018, *ApJ*, 863, 143, doi: [10.3847/1538-4357/aad32a](https://doi.org/10.3847/1538-4357/aad32a)
- Costagliola, F., Aalto, S., Rodriguez, M. I., et al. 2011, *A&A*, 528, A30, doi: [10.1051/0004-6361/201015628](https://doi.org/10.1051/0004-6361/201015628)
- Das, V., Crenshaw, D. M., Kraemer, S. B., & Deo, R. P. 2006, *AJ*, 132, 620, doi: [10.1086/504899](https://doi.org/10.1086/504899)
- den Brok, J. S., Chatzigiannakis, D., Bigiel, F., et al. 2021, *MNRAS*, 504, 3221, doi: [10.1093/mnras/stab859](https://doi.org/10.1093/mnras/stab859)
- den Brok, J. S., Bigiel, F., Sliwa, K., et al. 2022, *A&A*, 662, A89, doi: [10.1051/0004-6361/202142247](https://doi.org/10.1051/0004-6361/202142247)
- Eibensteiner, C., Barnes, A. T., Bigiel, F., et al. 2022, *A&A*, 659, A173, doi: [10.1051/0004-6361/202142624](https://doi.org/10.1051/0004-6361/202142624)
- Endres, C. P., Schlemmer, S., Schilke, P., Stutzki, J., & Müller, H. S. 2016, *Journal of Molecular Spectroscopy*, 327, 95
- Förster Schreiber, N. M., & Wuyts, S. 2020, *ARA&A*, 58, 661, doi: [10.1146/annurev-astro-032620-021910](https://doi.org/10.1146/annurev-astro-032620-021910)
- Fuente, A., Martín-Pintado, J., Cernicharo, J., & Bachiller, R. 1993, *A&A*, 276, 473
- Gallimore, J. F., Baum, S. A., & O’Dea, C. P. 1996a, *ApJ*, 464, 198, doi: [10.1086/177311](https://doi.org/10.1086/177311)
- Gallimore, J. F., Baum, S. A., O’Dea, C. P., & Pedlar, A. 1996b, *ApJ*, 458, 136, doi: [10.1086/176798](https://doi.org/10.1086/176798)
- García-Burillo, S., Combes, F., Usero, A., et al. 2014, *A&A*, 567, A125, doi: [10.1051/0004-6361/201423843](https://doi.org/10.1051/0004-6361/201423843)
- García-Burillo, S., Viti, S., Combes, F., et al. 2017, *A&A*, 608, A56, doi: [10.1051/0004-6361/201731862](https://doi.org/10.1051/0004-6361/201731862)
- García-Burillo, S., Combes, F., Ramos Almeida, C., et al. 2019, *A&A*, 632, A61, doi: [10.1051/0004-6361/201936606](https://doi.org/10.1051/0004-6361/201936606)
- Ginsburg, A., Koch, E., Robitaille, T., et al. 2019, *radio-astro-tools/spectral-cube: Release v0.4.5, v0.4.5*, Zenodo, doi: [10.5281/zenodo.3558614](https://doi.org/10.5281/zenodo.3558614)
- Hacar, A., Bosman, A. D., & van Dishoeck, E. F. 2020, *A&A*, 635, A4, doi: [10.1051/0004-6361/201936516](https://doi.org/10.1051/0004-6361/201936516)
- Harada, N., Sakamoto, K., Martín, S., et al. 2018, *ApJ*, 855, 49, doi: [10.3847/1538-4357/aaaa70](https://doi.org/10.3847/1538-4357/aaaa70)
- Harada, N., Thompson, T. A., & Herbst, E. 2013, *ApJ*, 765, 108, doi: [10.1088/0004-637X/765/2/108](https://doi.org/10.1088/0004-637X/765/2/108)
- Harada, N., Martín, S., Mangum, J. G., et al. 2021, *ApJ*, 923, 24, doi: [10.3847/1538-4357/ac26b8](https://doi.org/10.3847/1538-4357/ac26b8)
- Harris, C. R., Millman, K. J., van der Walt, S. J., et al. 2020, *Nature*, 585, 357, doi: [10.1038/s41586-020-2649-2](https://doi.org/10.1038/s41586-020-2649-2)
- Herbst, E. 1995, *Annual Review of Physical Chemistry*, 46, 27
- Herbst, E., Terzieva, R., & Talbi, D. 2000, *MNRAS*, 311, 869, doi: [10.1046/j.1365-8711.2000.03103.x](https://doi.org/10.1046/j.1365-8711.2000.03103.x)
- Högbom, J. A. 1974, *A&AS*, 15, 417
- Hollenbach, D., & McKee, C. F. 1980, *ApJL*, 241, L47, doi: [10.1086/183358](https://doi.org/10.1086/183358)
- Huang, K. Y., Viti, S., Holdship, J., et al. 2022, *arXiv e-prints*, arXiv:2202.05005. <https://arxiv.org/abs/2202.05005>

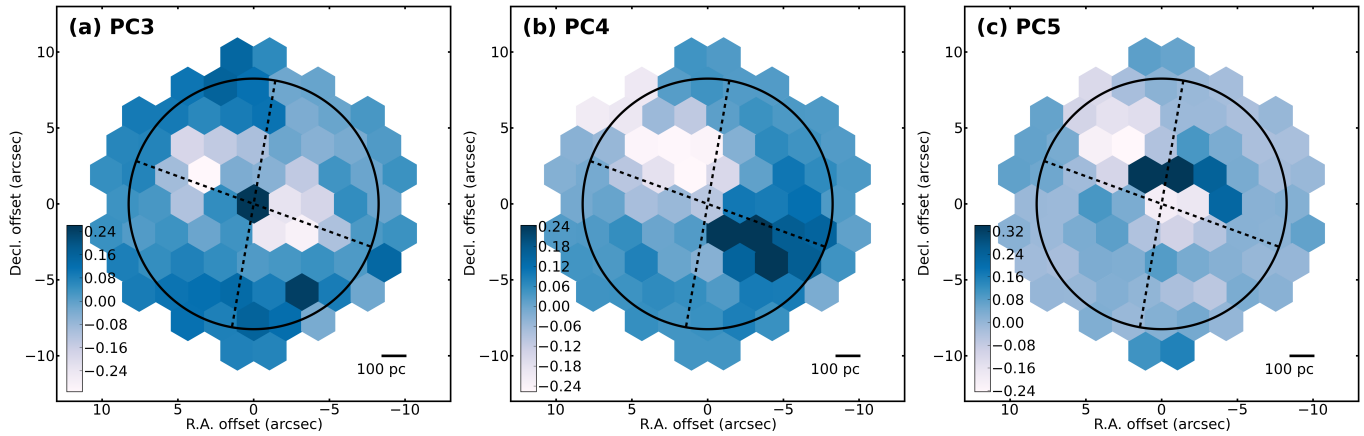


Figure 6. Minor PC maps; PC3 (a), PC4 (b), and PC5 (c). Two dashed lines crossing AGN position (Roy et al. 1998) denote approximate outer edges of ionized gas cones (Mingozi et al. 2019). Circle represents approximate field of view of Band 8 [C I] map (Saito et al. 2022), which is smallest among maps described in this paper.

- Izumi, T., Kohno, K., Martín, S., et al. 2013, PASJ, 65, 100, doi: [10.1093/pasj/65.5.100](https://doi.org/10.1093/pasj/65.5.100)
- Izumi, T., Nguyen, D. D., Imanishi, M., et al. 2020, ApJ, 898, 75, doi: [10.3847/1538-4357/ab9cb1](https://doi.org/10.3847/1538-4357/ab9cb1)
- Johnson, K. E., Brogan, C. L., Indebetouw, R., et al. 2018, ApJ, 853, 125, doi: [10.3847/1538-4357/aa9ff8](https://doi.org/10.3847/1538-4357/aa9ff8)
- Kauffmann, J., Goldsmith, P. F., Melnick, G., et al. 2017, A&A, 605, L5, doi: [10.1051/0004-6361/201731123](https://doi.org/10.1051/0004-6361/201731123)
- Kohno, K., Nakanishi, K., Tosaki, T., et al. 2008, Ap&SS, 313, 279, doi: [10.1007/s10509-007-9695-1](https://doi.org/10.1007/s10509-007-9695-1)
- Leroy, A. K., Hughes, A., Liu, D., et al. 2021a, arXiv e-prints, arXiv:2104.07665. <https://arxiv.org/abs/2104.07665>
- Leroy, A. K., Schinnerer, E., Hughes, A., et al. 2021b, arXiv e-prints, arXiv:2104.07739. <https://arxiv.org/abs/2104.07739>
- Martín, S., Martín-Pintado, J., & Viti, S. 2009, ApJ, 706, 1323, doi: [10.1088/0004-637X/706/2/1323](https://doi.org/10.1088/0004-637X/706/2/1323)
- Martín, S., Mauersberger, R., Martín-Pintado, J., Henkel, C., & García-Burillo, S. 2006, ApJS, 164, 450, doi: [10.1086/503297](https://doi.org/10.1086/503297)
- Martín, S., Mangum, J. G., Harada, N., et al. 2021, A&A, 656, A46, doi: [10.1051/0004-6361/202141567](https://doi.org/10.1051/0004-6361/202141567)
- May, D., & Steiner, J. E. 2017, MNRAS, 469, 994, doi: [10.1093/mnras/stx886](https://doi.org/10.1093/mnras/stx886)
- McMullin, J. P., Waters, B., Schiebel, D., Young, W., & Golap, K. 2007, in Astronomical Society of the Pacific Conference Series, Vol. 376, Astronomical Data Analysis Software and Systems XVI, ed. R. A. Shaw, F. Hill, & D. J. Bell, 127
- Meier, D. S., & Turner, J. L. 2005, ApJ, 618, 259, doi: [10.1086/426499](https://doi.org/10.1086/426499)
- Meijerink, R., & Spaans, M. 2005, A&A, 436, 397, doi: [10.1051/0004-6361:20042398](https://doi.org/10.1051/0004-6361:20042398)
- Mendes, M. B., Buhr, H., Berg, M. H., et al. 2012, ApJL, 746, L8, doi: [10.1088/2041-8205/746/1/L8](https://doi.org/10.1088/2041-8205/746/1/L8)
- Michiyama, T., Iono, D., Nakanishi, K., et al. 2020, ApJ, 895, 85, doi: [10.3847/1538-4357/ab88a5](https://doi.org/10.3847/1538-4357/ab88a5)
- Mingozi, M., Cresci, G., Venturi, G., et al. 2019, A&A, 622, A146, doi: [10.1051/0004-6361/201834372](https://doi.org/10.1051/0004-6361/201834372)
- Mukherjee, D., Bicknell, G. V., Sutherland, R., & Wagner, A. 2016, MNRAS, 461, 967, doi: [10.1093/mnras/stw1368](https://doi.org/10.1093/mnras/stw1368)
- Nakajima, T., Takano, S., Kohno, K., Harada, N., & Herbst, E. 2018, PASJ, 70, 7, doi: [10.1093/pasj/psx153](https://doi.org/10.1093/pasj/psx153)
- Nakajima, T., Takano, S., Kohno, K., et al. 2015, PASJ, 67, 8, doi: [10.1093/pasj/psu136](https://doi.org/10.1093/pasj/psu136)
- Pearson, K. 1901, The London, Edinburgh, and Dublin Philosophical Magazine and Journal of Science, 2, 559, doi: [10.1080/14786440109462720](https://doi.org/10.1080/14786440109462720)
- Pety, J., Guzmán, V. V., Orkisz, J. H., et al. 2017, A&A, 599, A98, doi: [10.1051/0004-6361/201629862](https://doi.org/10.1051/0004-6361/201629862)
- Rangwala, N., Maloney, P. R., Glenn, J., et al. 2011, ApJ, 743, 94, doi: [10.1088/0004-637X/743/1/94](https://doi.org/10.1088/0004-637X/743/1/94)
- Roy, A. L., Colbert, E. J. M., Wilson, A. S., & Ulvestad, J. S. 1998, ApJ, 504, 147, doi: [10.1086/306071](https://doi.org/10.1086/306071)
- Saito, T., Takano, S., Harada, N., et al. 2022, arXiv e-prints, arXiv:2203.01355. <https://arxiv.org/abs/2203.01355>
- Sakamoto, K., Martín, S., Wilner, D. J., et al. 2021, ApJ, 923, 240, doi: [10.3847/1538-4357/ac29bf](https://doi.org/10.3847/1538-4357/ac29bf)
- Scannapieco, E., & Oh, S. P. 2004, ApJ, 608, 62, doi: [10.1086/386542](https://doi.org/10.1086/386542)
- Schinnerer, E., Eckart, A., Tacconi, L. J., Genzel, R., & Downes, D. 2000, ApJ, 533, 850, doi: [10.1086/308702](https://doi.org/10.1086/308702)

- Stuber, S. K., Saito, T., Schinnerer, E., et al. 2021, *A&A*, 653, A172, doi: [10.1051/0004-6361/202141093](https://doi.org/10.1051/0004-6361/202141093)
- Sturm, E., González-Alfonso, E., Veilleux, S., et al. 2011, *ApJL*, 733, L16, doi: [10.1088/2041-8205/733/1/L16](https://doi.org/10.1088/2041-8205/733/1/L16)
- Tafalla, M., Usero, A., & Hacar, A. 2021, *A&A*, 646, A97, doi: [10.1051/0004-6361/202038727](https://doi.org/10.1051/0004-6361/202038727)
- Takano, S., Nakajima, T., & Kohno, K. 2019, *PASJ*, 71, S20, doi: [10.1093/pasj/psz020](https://doi.org/10.1093/pasj/psz020)
- Takano, S., Nakajima, T., Kohno, K., et al. 2014, *PASJ*, 66, 75, doi: [10.1093/pasj/psu052](https://doi.org/10.1093/pasj/psu052)
- Tosaki, T., Kohno, K., Harada, N., et al. 2017, *PASJ*, 69, 18, doi: [10.1093/pasj/psw122](https://doi.org/10.1093/pasj/psw122)
- Veilleux, S., Maiolino, R., Bolatto, A. D., & Aalto, S. 2020, *A&A Rv*, 28, 2, doi: [10.1007/s00159-019-0121-9](https://doi.org/10.1007/s00159-019-0121-9)
- Virtanen, P., Gommers, R., Oliphant, T., et al. 2020, *Nature Methods*, 17, 261, doi: [10.1038/s41592-019-0686-2](https://doi.org/10.1038/s41592-019-0686-2)
- Visser, R., van Dishoeck, E. F., & Black, J. H. 2009, *A&A*, 503, 323, doi: [10.1051/0004-6361/200912129](https://doi.org/10.1051/0004-6361/200912129)
- Viti, S., Jimenez-Serra, I., Yates, J. A., et al. 2011, *ApJL*, 740, L3, doi: [10.1088/2041-8205/740/1/L3](https://doi.org/10.1088/2041-8205/740/1/L3)
- Walter, F., Bolatto, A. D., Leroy, A. K., et al. 2017, *ApJ*, 835, 265, doi: [10.3847/1538-4357/835/2/265](https://doi.org/10.3847/1538-4357/835/2/265)